Optimum Heat Treatment Conditions Determination for Mg-Diffused MgB$_2$

Ö. ÇIÇEK* AND K. YAKINCI

Department of Basic Engineering Sciences, Faculty of Engineering and Natural Sciences, İskenderun Technical University, Central Campus, Meydan District, Ibrahim Karaoglanoglu Street, No: 56/5, 31200, Hatay, Turkey

MgB$_2$ superconducting pellets were synthesized by the Mg diffusion method. Different heat treatment temperatures and times were applied for synthesis to determine optimum conditions. The phase structure of the samples was investigated by X-ray diffraction measurements. MgB$_2$ lattice parameters, MgO fractions, and crystal sizes were calculated. It was observed from the scanning electron microscope images that the grains were well connected and the grain sizes were homogeneous after heat treatment at 650°C and 12 h. As a result of magnetization measurements, it was determined that the critical temperature of the samples that were heat-treated at 650 and 700°C for 6 and 12 h showed close values, and the transition intervals were sharp. The critical current density values calculated according to the Bean model were found to be around 10^4 A/cm^2 for 625°C samples and increased to 10^5 A/cm^2 for 650 and 700°C samples. The highest critical current density value under 0 T at 20 K was obtained as 1.58×10^5 A/cm^2 for the 700°C for 6 h sample. It was determined that the irreversibility field values determined according to the 100 A/cm^2 criterion were close for 650 and 700°C heat treatments. The pinning mechanism analyzed by the Dew-Hughes approach was detected as grain boundary pinning in 650 and 700°C samples. It was shown that the minimum temperature for the heat treatment to be applied for the Mg diffusion method should be 650°C, and the extended heat treatment duration made no serious difference.

topics: MgB$_2$ bulks, Rietveld refinement, $J_{c,\mathrm{mag}}$, grain boundary pinning

1. Introduction

Since magnesium diboride (MgB$_2$) was reported as a metallic superconductor by J. Nagamatsu et al. [1] in 2001, much work has been done to date to improve the parameters of MgB$_2$ to make it suitable for various applications [2–6]. Interesting features of the MgB$_2$ superconductor are (i) simple chemical structure, (ii) relatively easy production [7], (iii) low chemical cost [8], (iv) ability to work as polycrystalline, (v) ability to be produced in different shapes and sizes (bulk, cylinder, ring, wire, strip) [9, 10], (vi) grain boundaries as pinning centers [11], (vii) ability to trap larger magnetic fields [12]. MgB$_2$-based superconducting materials for applications in energy, electronics, medicine, and particle physics, such as magnetic resonance imaging (MRI) [13–16], fault current limiters (FCL), superconducting quantum interference devices (SQUIDs) [17–19], motors, generators, etc., have been produced as bulks [20], tapes [21], wires [22], and films [23, 24]. In addition to all the above-mentioned properties, MgB$_2$ is a lightweight material, making it a valuable superconductor, especially in space applications and other applications requiring low-mass materials [25, 26]. However, the sharp decrease in the critical current density (J_c) with increasing magnetic field is a problem that limits the use of MgB$_2$ in applications in high magnetic fields and has been the subject of studies. Well-developed MgB$_2$ wires/cables/tape are required for most applications, and different approaches have been proposed to improve the transport properties of MgB$_2$ wire/cable/tape. Studies aimed at improving transport properties have focused on improving pinning centers and/or increasing their density to increase J_c. The conducted research showed that thermal treatment in the high-pressure isostatic press (HIP) allows for an increase in the density of high-field pinning centers, an increase in the density of the superconducting material, and significant improvement of the connections between grains [15, 27–28].

The most popular topic for creating artificial pinning centers has been the doping or addition of MgB$_2$. Chemical doping or addition [29] are simple and effective methods to enhance superconducting properties under the high fields to which MgB$_2$ may be exposed in practical applications. Many dopants were tried for MgB$_2$ and most of them

TABLE I

Sample codes, code-related heat treatment (HT) conditions, bulk density and the relative densities of the samples.

Sample code	HT conditions	d [g/cm^3]	Relative d [%]
D625-06	at 625°C for 6 h	1.0149	38.74
D625-12	at 625°C for 12 h	1.4219	54.27
D650-06	at 650°C for 6 h	1.5813	60.36
D650-12	at 650°C for 12 h	1.6265	62.08
D700-06	at 700°C for 6 h	1.7037	65.03
D700-12	at 700°C for 12 h	1.6304	62.23

had a negative effect on $J_c(B)$. The most studied dopants that increase $J_c(B)$ are MgB$_4$ [30], Dy$_2$O$_3$ [31], SiC [32, 33], B$_4$C [34], nano-carbon [35], carbon–nanotubes [36], and oxides. Doping of carbon and carbon-containing dopants [37, 38] into MgB$_2$ has been shown to improve H_{irr}, H_{c2}, and J_c at high magnetic fields [39]. This improvement situation is interpreted as the carbon atom being able to replace the boron atom in the MgB$_2$ structure because their atomic radii are close, thus creating defects that can serve as pinning centers.

The fact that grain boundaries in MgB$_2$ act as pinning centers has led to studies on grain boundary improvement as well as doping. In general, the development of grain boundaries as pinning centers has been attempted by modifying the MgB$_2$ synthesis procedures. The MgB$_2$ superconductor has generally been produced by ex-situ and in-situ techniques. In the in-situ method, the precursor powders are brought to the desired form by mixing them in appropriate proportions according to the chemical formula, and then subjected to heat treatment to cause a chemical reaction. In this synthesis method, during the heat treatment, Mg grains melt with the liquid–solid reaction and disperse into B grains. The in-situ method provides good superconducting connectivity and more effective results in doping. However, the disadvantage of this method is that it results in a lower packing ratio of around 50% [40, 41]. In cases where the process is exactly the opposite, the production method is called ex-situ; first, the MgB$_2$ phase is obtained from the precursor powders, and then it is put into the desired form. Although the ex-situ method provides homogeneous and non-porous structures with a packing ratio of around 74% [42], these structures are accompanied by the disadvantage of low critical current density due to weak superconducting connectivity. The Mg diffusion method, which falls into the in-situ synthesis category, has the advantage of obtaining dense samples of the ex-situ method, in addition to the good grain coupling advantage [43] of the in-situ method. The density of MgB$_2$ bulks produced by the Mg diffusion method is reported as 1.95 g/cm^3 [44]. In the

same study, it was reported that the synthesized MgB$_2$ has $T_c = 38.1$ K and $J_c(B=0$ T, $T=10$ K$) = 5.3 \times 10^5$ A/cm^2. Additionally, Ueda et al. [45] obtained $J_c(B=0$ T, $T=20$ K$) = 8.6 \times 10^5$ A/cm^2 as a result of heat treatment at 800°C for 60 h, which was explained by small grains of 30–100 nm in size, good grain connectivity, and an increase in effective current transfer. For optimizing J_c, modifying the heat treatment variables is an effective way. Optimal determination of heat treatment variables that strengthen grain bonding and increase grain boundary density can result in high $J_c(B)$ [46]. Recent research showed that the high density of the in-situ superconducting MgB$_2$ material allows for the acceleration of the synthesis reaction and the formation of the superconducting MgB$_2$ phase [47]. On the other hand, the conducted experiments showed that the high density of the boron layer leads to a significant slowdown of Mg diffusion in the samples made by using internal magnesium diffusion (IMD) technology [48, 49].

This study aimed to determine the optimum heat treatment conditions for the Mg diffusion method by using specially shaped Mg and B pellets prepared under the same conditions. Therefore, in this study, microstructural and magnetic examination of bulk MgB$_2$ samples subjected to Mg diffusion heat treatment at 625, 650, and 700°C for 6 and 12 h was carried out.

2. Experimental methods

The samples examined in this study, aimed at Mg diffusion, were prepared from commercially available magnesium powder (Pavezyum company magnesium, 99%, particle size < 44 μm) and amorphous nano-boron powder (Pavezyum company nano-sized amorphous elemental boron, 99%, particle size < 400 nm). Starting powders were weighed according to the chemical ratio Mg : B $= 1 : 2$. Boron powder was pressed isostatically under 100 MPa pressure in a specially shaped pressing mold. The same method was used to obtain the Mg pellet. The Mg pellet was placed on top of the B pellet as an Mg diffusion source and then subjected to heat treatment (HT) under an Ar atmosphere temperatures 625, 650, and 700°C for 6 and 12 h using an Nb-sheeted Al$_2$O$_3$ crucible and finally left to cool in the furnace. The obtained samples were coded as given in Table I. Sample codes start with the letter "D" which stands for diffusion; the first numerical part of the code refers to the HT temperature, and the second numerical part refers to the HT duration. Contact with Mg surfaces of the heat-treated samples was washed with acetone and dried. Pieces of appropriate size were cut from the samples for various analyses. Dimensions and weight measurements were taken of these cut pieces using a micrometer and a precision scale, and the

density of the pieces was calculated. Calculations of relative bulk density, also called packing ratio, were performed using the theoretical density of MgB_2. X-ray diffraction (XRD) measurements were made on the Mg contact surfaces of equal-sized pieces cut from the samples. The phases formed in the samples were determined using Cu K_α X-ray diffraction with the Rigaku powder diffractometer system. The MgB_2 pieces were scanned from the surface between $20°$ and $90°$ with an angular step of $0.01°$. It was found that the patterns obtained in the XRD results corresponded to the hexagonal MgB_2 and cubic MgO structure. Rietveld refinement with the FullProf software was used to further investigate the phase composition and calculate lattice parameters. For the two-phase Rietveld purification, the pseudo-Voigt function was preferred to simulate the peak profiles in the pattern. The crystal sizes and strain of the samples were calculated using the Williamson–Hall (WH) equation [50] based on the XRD results. The microstructure of the samples was observed using scanning electron microscopy from the diffusion surface of the pellet pieces. The magnetization of the samples against the applied magnetic field was measured using the Physical Property Measurement System (PPMS) up to 5 T at 10, 20, and 30 K. The critical current densities of the samples (J_c in [A/cm^2]) were calculated using the extended Bean model [51]

$$J_c = \frac{20\Delta M}{a - \frac{a^2}{3b}}, \tag{1}$$

where $\Delta M = M^+ - M^-$ (in [emu/cm^3]) is the magnetization loop width, and a and b ($a<b$, in [cm]) are the cross-sectional dimensions of the bar-shaped sample. Throughout our study, the magnetic field was applied parallel to the sample surface. For the examined samples, the magnetic field-dependent flux pinning mechanisms were analyzed through $J_c(H_{app}/H_{irr})$ graphs (where $\mu_0 H_{irr}$ is determined from the criteria $J_c = 100$ A/cm^2). The temperature of the transition from the superconducting state to the normal state and the width of this transition were determined from the temperature dependence of the magnetization measurement under 0.01 T.

3. Results and discussions

3.1. Packing ratio analysis

The bulk densities of the samples were calculated from the sample pieces prepared for characterization measurements, using a micrometer and a weighing scale. When calculating the relative density d using the relation [52]

$$\text{relative } d\,[\%] = \frac{\text{bulk } d}{\text{theoretical } d} \times 100, \tag{2}$$

we assume that the theoretical density of MgB_2 is 2.62 g/cm^3 [53]. The densities and relative bulk densities of the samples are given in Table I.

When the relative densities — also known as packaging factors [54] — were examined, an increasing packaging ratio was obtained with increasing heat treatment temperature and duration. In other words, it has been shown that increasing the HT temperature and duration produces fewer pores and more MgB_2 phase in the same volume. However, when the values of the 650 and 700°C samples are examined more closely, we can say that the rate of increase in the packaging ratio was decreasing and that a plateau began to form in the packaging rate with increasing temperature and time. The fact that the curve started to plateau showed that 650°C was a sufficient temperature to create the optimum packaging rate that could be achieved in our samples produced by Mg diffusion. In the literature, a higher packaging was achieved compared to MgB_2 samples ($\sim 50\%$) produced without applying pressure during heat treatment by the in-situ method [55]. Although the packing factor for MgB_2 samples synthesized by the ex-situ method was higher (74%) in the literature, it has been reported that the samples have a weak grain connection [42]. The samples produced in this study have a higher packing rate than those from the in-situ method, i.e., close to those of the ex-situ method. Moreover, our samples also have the advantage of better grain connection than those of the in-situ method. In light of these findings, it was evaluated that the MgB_2 layer density in the measured sample pieces was even above 65%. The measured sample pieces were cut from specially shaped samples with a thickness of ≈ 2 mm to include the Mg diffusion surface. For this reason, it is thought that the entire volume of these pieces does not consist only of MgB_2. In other words, since the volume used in this calculation actually contained both MgB_2 and some unreacted B, the densities calculated above were considered to be lower than their actual values.

3.2. XRD analysis

Immediately after heat treatment, equal-sized pieces were cut from the samples, and XRD measurements were carried out at room temperature by scanning the surface of these pieces between $20°$ and $90°$ with a step of $0.01°$ (see Fig. 1). The expected impurity phase in MgB_2 is MgO resulting from the high reactivity of metallic Mg [56]. In Fig. 1, in all peaks for each sample, it was seen that the main phase was well-developed MgB_2 with a small amount of MgO formation. The peak corresponding to the MgO (220) reflection at $2\theta \approx 63°$ is the second most intense peak of MgO and was observed in all samples. However, at $2\theta \approx 42.8°$, the peak corresponding to the MgO (200) reflections was obscured
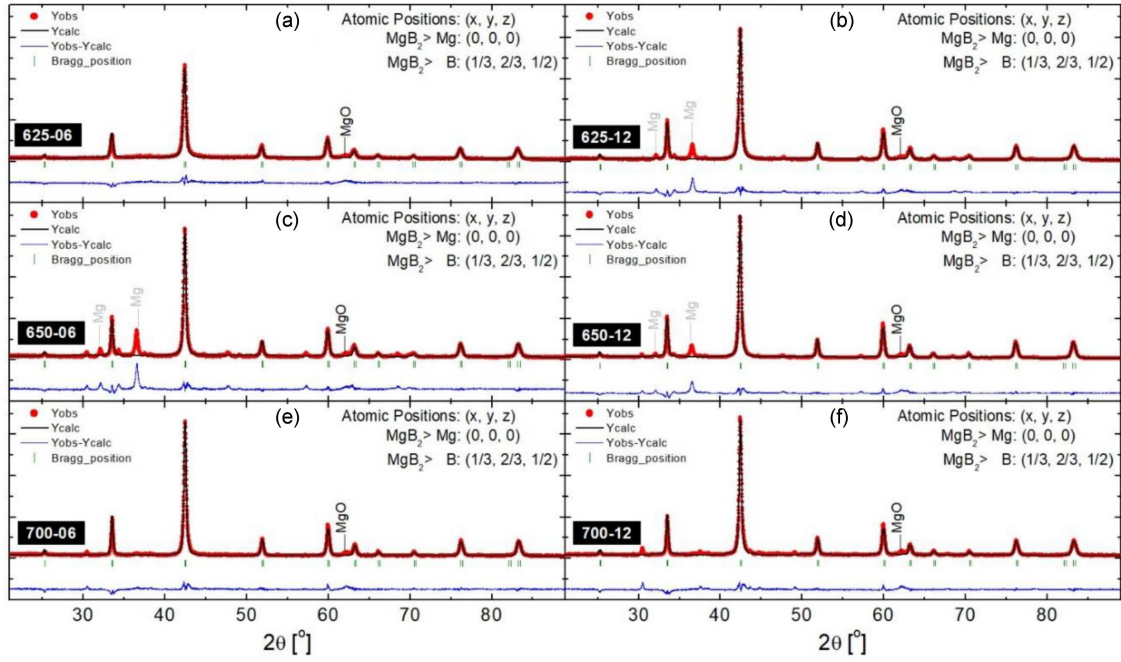
Fig. 1.   Refinement results (black solid line) and observed XRD patterns (red full circle) of the samples.

TABLE II

Lattice parameters, cell volume, MgO phase fraction obtained from Rietveld refinement, and MgO relative intensity.

	D625-06	D625-12	D650-06	D650-12	D700-06	D700-12
$a = b$ of MgB_2 [Å]	3.08642	3.08458	3.08485	3.08639	3.08277	3.08395
c of MgB_2 [Å]	3.52547	3.52107	3.52235	3.52235	3.52063	3.52157
c/a	1.14225	1.14150	1.14182	1.14125	1.14203	1.14190
Cell volume of MgB_2	29.08	29.01	29.03	29.07	28.98	29.01
MgO fraction from Rietveld refinement	1.83	1.37	1.41	1.28	1.40	1.60
MgO relative intensity	1.25	1.05	1.26	1.07	1.16	1.29

by the main peak of MgB_2. Additionally, Mg peaks were observed in samples D625-12, D650-06, and D650-12, regardless of the temperature and duration of heat treatment. If the XRD measurements were performed on powdered samples, it would be expected that the Mg peaks would decrease or even disappear with increasing temperature and duration of heat treatment. In this case, since the XRD measurements were taken on the surface of the pellet pieces in contact with Mg, and since Mg peaks were observed randomly in the samples against the temperature-duration increase, it was evaluated that these Mg peaks resulted from unreacted melted Mg remaining as contamination on the surface of the sample after heat treatment.

Rietveld refinements were used to further investigate the composition of the phase and calculate lattice parameters. Rietveld refinements were carried out using the Fullprof software [57]. The pseudo-Voigt function was chosen to simulate the peak profile. The lattice structure of MgB_2 belongs to the $P6/mmm$ space group. The unit of the MgB_2 structure is an asymmetric unit in which the Mg atoms are in the $(0, 0, 0)$ position, and the B atoms are in the $(1/3, 2/3, 1/2)$ position [58]. The lattice structure of MgO belongs to the space group $Fm\text{-}3m$. In this structure, Mg atoms are in the $(0, 0, 0)$ position and B atoms are in the $(1/2, 1/2, 1/2)$ position. This information was defined where necessary in the program established for Rietveld refinement. In addition, the positions and occupancy parameters of the relevant atoms were kept constant at their nominal values. Background matching was first performed before starting to refine the XRD patterns of the produced samples. Then, the scale factor, global parameters, Caglioti parameters (U, V, W), and peak shape were improved. During pre-refinement, impurity peaks were excluded. The MgB_2 lattice parameters were obtained by this single-phase purification. Two-phase purification was used to determine the MgO fraction. A low fit parameter (χ^2) was the goal to achieve agreement between experimental
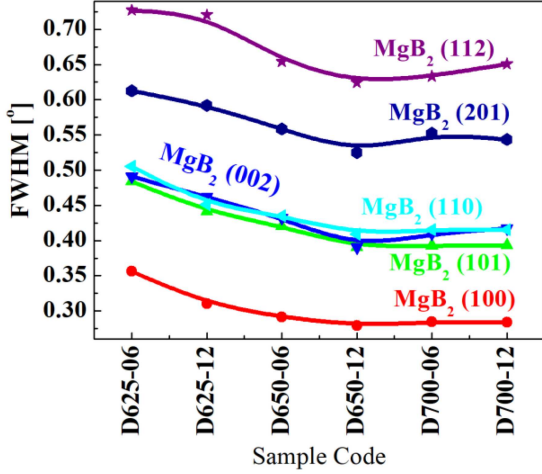
Fig. 2. FWHM values of peaks (100), (101), (002), (110), (201), and (112) of the MgB$_2$ phase samples.

and calculated data. The resulting plots for single-phase refinement are shown in Fig. 1. The difference between the original measurement results (red circles) and the calculated model (black line) are marked by the blue line. The Bragg reflections for MgB$_2$ are shown as green bars.

The MgB$_2$ lattice parameters, c/a ratios, and cell volume values obtained by single-phase treatment are given in Table I. The average lattice parameters reported in the literature for pure MgB$_2$ samples are $a = 3.08485$ Å and $c = 3.52634$ Å [59–64]. In all samples produced in this study, the lattice parameter a was determined in the range of 3.0828–3.0864 Å, and the lattice parameter c was determined in the range of 3.5206–3.5255 Å. Since no changing feature compatible with the changing HT temperature and time can be detected in these intervals, and the magnitude of the changes was at a maximum rate of 0.12% for the lattice parameter a and 0.14% for the lattice parameter c, thinking about such aspect of a change can be ignored. Thus, the lattice parameters can be considered to remain constant. The ratio c/a and cell volume also remained constant and are consistent with the literature [59].

When examining Table II in terms of the phase percentages obtained as a result of refinement, the lowest MgO phase percentage was obtained in D650-12. Since an Ar atmosphere was used in the heat treatment process, it is thought that the reason for the existence of the MgO phase was the oxidation of the samples prepared before heat treatment and/or the purity of the rapidly oxidized Mg powder. The fact that the MgO phase volume fraction was limited to a maximum of 1.83% for all samples was interpreted as taking samples for XRD analysis immediately after heat treatment, without waiting. It has been observed that this proportional change, which occurs within a very small range, has

no relationship with the temperature and duration of heat treatment. The relative density fraction of the MgO phase was also calculated for control purposes using [65]

$$D_{\mathrm{MgO}}\,[\%] = \frac{I_{\mathrm{MgO}(220)}}{\left(\sum I_{\mathrm{MgB}_2(hkl)}\right) + I_{\mathrm{MgO}(220)}} \times 100, \quad (3)$$

where I is the height of the XRD peak and (hkl) are the Miller indices. The summation in (3) is equal to the sum of (001), (100), (101), (002), (110), (102), (111), (200), (201), (112) peaks heights of MgB$_2$. When the results calculated for each sample according to this formula were compared with the MgO fractions obtained as a result of Rietveld purification, it was observed that they showed a parallel trend (see Table II). According to both results, the lowest MgO phase ratio was observed in sample D650-12.

Another important parameter that contains information about the crystallographic structure is the peak width (FWHM — full width at half maximum) [66]. Here, to compare the FWHM values, the (100), (101), (002), (110), (201), and (112) reflection peaks of the MgB$_2$ phase were evaluated. The peaks belonging to the (001), (111), and (200) reflections of MgB$_2$ were excluded from the evaluation because they increased the margin of error in the FWHM calculation due to their low peak intensities. A narrowing trend was observed in the MgB$_2$ peaks assessed with increasing HT temperature and duration, and it was determined that each peak converged to certain values (see Fig. 2). This suggested that the crystal size reached its optimum value at 650°C.

At this point, the Williamson–Hall (WH) equation was used to calculate the crystal size and strain in the samples. The Williamson–Hall equation combines the Scherrer equation, which determines the particle effect, and the Stokes–Wilson equation, which gives the micro stress. WH graphs created according to the dependence of $\beta \cos(\theta)$ on $4\sin(\theta)$ are shown in Fig. 3. The slope value of these graphs gives the strain, and the y-axis intersection point allows us to calculate the crystal size. We use the relation

$$\beta_{hkl} \cos(\theta) = \frac{K\lambda}{D} + 4\varepsilon \sin(\theta), \quad (4)$$

where β is the FWHM value of XRD peaks, $K = 0.94$ is the shape factor of the particles, θ is the diffraction angle of the Miller indices, $\lambda = 0.15406$ nm is the wavelength of X-ray, ε is the lattice strain, and D is the crystallite size. Using the WH plots given in Fig. 3, the crystal size and strain values obtained by the procedure mentioned above are given in Fig. 4.

As can be seen, the optimum crystal size was reached as a result of applying HT for 12 h at 650°C. When the strain values obtained with WH were examined, an increasing tension was observed with increasing duration at 625°C, while a decreasing trend
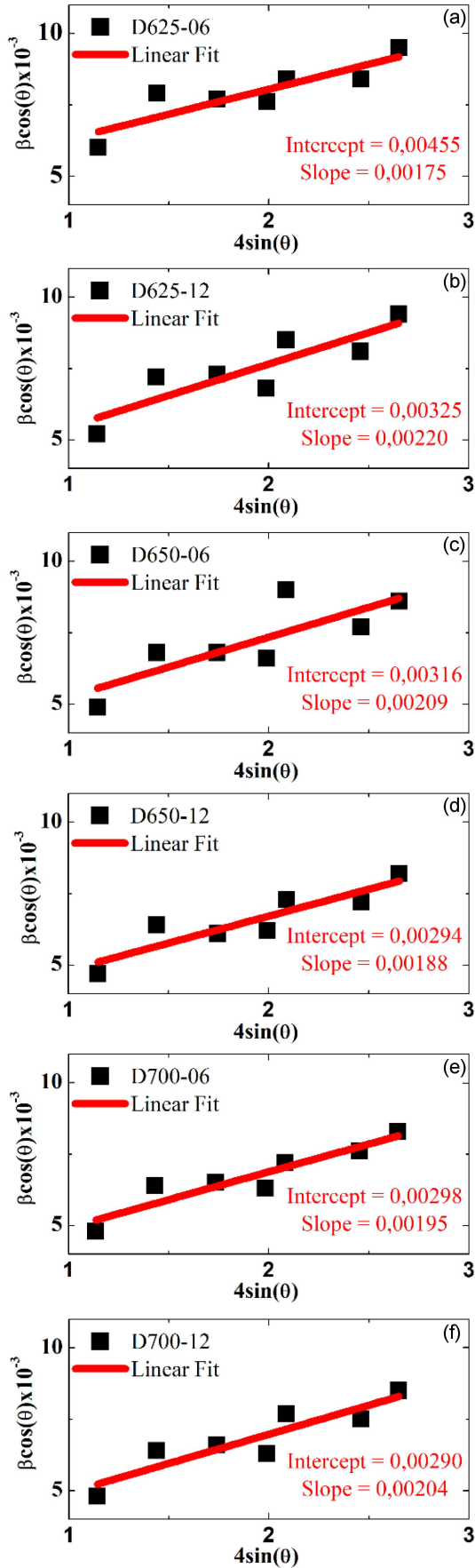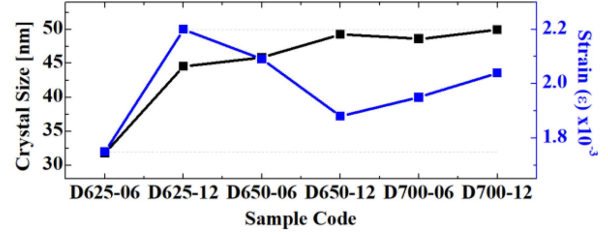
Fig. 4. Crystal size and lattice stress according to Williamson–Hall plots of the samples.

was observed with increasing duration at 650°C. The minimum strain value was obtained for 12-h HT at 650°C. Afterward, it was observed that it increased at a slower rate with increasing temperature and duration. In [67], the decrease in crystal size increases the scattering of electrons and, therefore, increases the upper critical field (H_{c2}) and resistivity value. It has also been reported that decreasing the crystallite size reduces T_c [68]. Evaluating from this perspective, we can say that the temperature 650°C of HT was the optimum value at which the minimum strain value and optimum crystal size were achieved during sample preparation. Extending the HT time also had a positive effect.

3.3. SEM analysis

Scanning electron microscope (SEM) images taken from the surfaces of the samples heat-treated for 12 h were shown in Fig. 5. It was observed that in all samples, the grains were irregularly shaped and randomly oriented. The microstructure of sample D625-12 showed low connectivity between grains of different sizes at the micron scale. The general structure in this sample was found to be very porous and loose. In sample D650-12, it was observed that grains with more homogenized sizes at the micron scale were formed and that the grains were more rounded and smooth at the edges. When examined more closely, it was observed that coalescence between the particles also occurred, and the pores decreased. Based on this observation, it was concluded that sintering has taken place. On the other hand, better fused locally melted structures were observed in sample D700-12 compared to sample D650-12. In Fig. 4, in which the results obtained from the WH plots were displayed, the crystal size heat treated for 12 h at 650°C reached the maximum value, and this size remained almost constant with a slight increase in 12-h HT applications at 700°C. The trend in the grain size change we observed in SEM images was found to be similar to the change in crystal sizes calculated by WH. When high-magnification SEM images were examined, the fact that this porous structure was observed in certain proportions in our samples was attributed to

Fig. 3. Williamson–Hall plots of the samples.

the fact that the SEM images were taken as they were from the Mg-diffusion surface of the samples (without cutting or polishing).

3.4. Magnetization analysis

The temperature-dependent measurements of the magnetic moment $M(T)$ of the samples under the applied constant magnetic field (0.01 T) were examined. The $T_{c,\text{onset}}$ values were determined as the first deviation point from the normal state, and the $T_{c,\text{offset}}$ values were determined as the point of becoming completely superconducting. The critical transition of the samples heat-treated for 6 h and 12 h are shown in Fig. 6a and Fig. 6b, respectively. In both graphs, in order to examine the turning points more closely, the first deviation region from the normal state and the transition regions to the completely superconducting state were marked in yellow. Zoomed-in versions of these regions are shown in insets. For both 6-h and 12-h samples, it was observed that samples heat-treated at 625°C
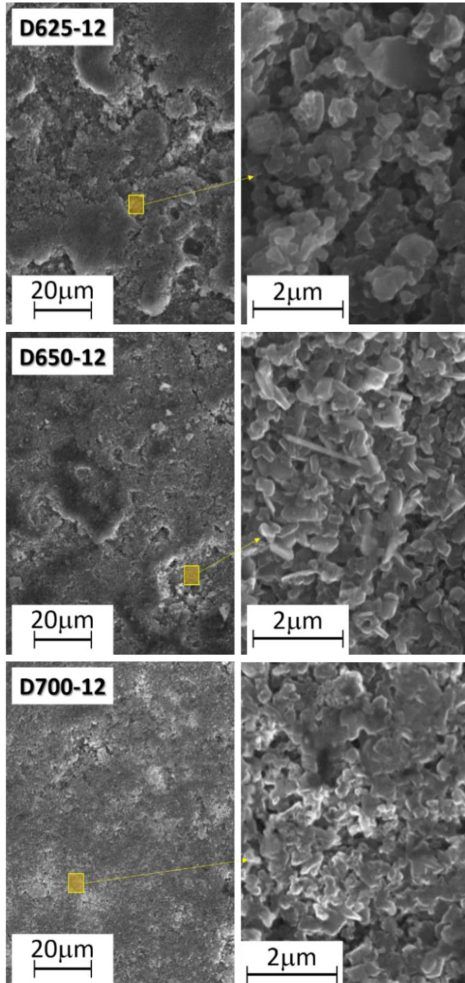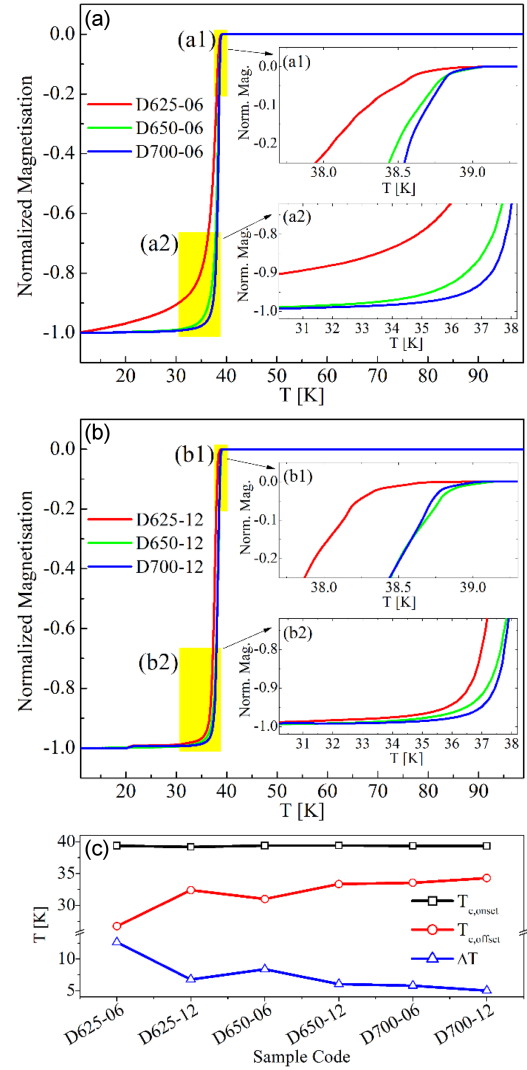

Fig. 5. SEM images of samples heat-treated for 12 h.

Fig. 6. Normalized magnetization dependence on temperature of (a) the 6-h heat-treated samples and (b) the 12-h heat-treated samples; (c) $T_{c,\text{onset}}$, $T_{c,\text{offset}}$, and ΔT plots of the samples.

transitioned at lower temperatures, and their transition ranges were wider. Among the 6-h samples, the 650°C sample starts transitioning at almost the same temperature as the 700°C sample, while the transition range is slightly wider in the 650°C sample. Among the 12-h samples, it was observed that the 650°C sample started transitioning at a slightly higher temperature than the 700°C sample, while it became fully superconducting at a slightly lower temperature. As can be easily seen in Fig. 6c, the 650°C and 700°C samples have close critical temperature values and a narrow transition range. The presence of such a narrow phase transition indicates that these samples have better superconductivity properties than the 625°C samples. This narrow transition also indicates that the sample is a single superconducting phase. Based on the transition width, it can be said that 6 h of HT application at 625°C is insufficient, while 12 h of HT
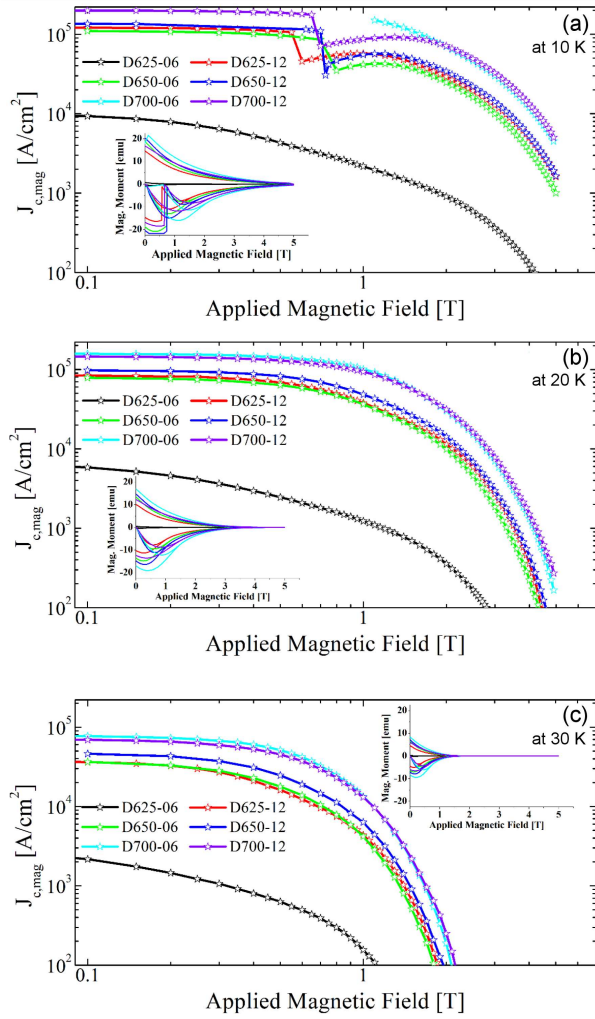
330

Fig. 7. Magnetic J_c graphs of the samples calculated with the Bean model at (a) 10 K, (b) 20 K, (c) 30 K. The relevant magnetization cycles for which this calculation was made are shown in insets.

application provides partial improvement. However, despite the small differences between the 650°C and 700°C samples, the sharp phase transition of these samples indicates that the samples exhibit a good degree of homogeneity. This conclusion was parallel to the conclusion that the 650°C and 700°C samples, which we obtained from SEM images, exhibit similar structures.

The magnetic field dependences of the magnetic critical current density $(J_{c,\text{mag}})$ of the samples were obtained from the widths of the magnetization hysteresis loops taken from bar-shaped samples. The magnetic critical current density $(J_{c,\text{mag}})$ was calculated using the extended Bean model [51] defined in (1). The magnetic critical current density curves calculated from $M(H)$ measurements are shown in Fig. 7a for 10 K, Fig. 7 b for 20 K, and Fig. 7c for 30 K. In the calculations performed at 10 K in the samples synthesized at 650°C and 700°C, the sharp changes observed in the low magnetic field

region (around 1 T) were due to a magnetic flux jump. This was because high $J_{c,\text{mag}}$ and low heat capacity cause a localized movement of the magnetic flux, causing flux jumps in the superconducting material [69].

The calculated values of $J_{c,\text{mag}}$ were found to be comparable to the literature (see Fig. 7). The self-field $J_{c,\text{mag}}$ is an important criterion for MgB$_2$. In [70], it was reported that the self-field J_c values at 20 K for MgB$_2$ produced from B powder processed in different ways were between 0.712×10^5 A/cm^2 and 1.555×10^5 A/cm^2. When the corresponding graph in this study was examined closely, it was determined that the J_c value decreased to 100 A/cm^2 for all samples around 3.5 T. In another study [52], in which the ex-situ and in-situ techniques were applied in combination, the highest self-field J_c value at 20°C was reported as 3.48×10^5 A/cm^2. In the same study, the self-field J_c value of the sample produced using only the in-situ technique was reported as 2.98×10^5 A/cm^2. In this study, when the J_c change under increasing magnetic field was examined closely, it was observed that the J_c values of all samples decreased to 100 A/cm^2 around 4.5–5 T. In the samples produced in this study, the highest critical current density at 20 K was 1.58×10^5 A/cm^2 (D700-06), which was found to be comparable to literature values. In addition, the decrease in the J_c value to 100 A/cm^2 occurred around 4.5 T at 20 K, which was consistent with the results obtained by Dadiel et al. [52].

When the J_c plots were examined, it was observed that during HT for 6 h at 625°C, very low J_c values were obtained compared to all others. In addition, the rapid depreciation of J_c with increasing magnetic field clearly showed that these HT conditions create a very low rate of the MgB$_2$ superconducting phase. It was observed that 12 h of HT at 625°C provided a significant improvement compared to 6 h of heat treatment. In this case, it can be said that 6 h of HT at 625°C is insufficient, but with extended HT duration, a higher rate of the MgB$_2$ superconducting phase was formed, which was compatible with other samples.

When the 6-h and 12-h HT data at 650°C were compared to each other, it was seen that the 12-h heat treatment improves the sample properties and gives better J_c results. The improved J_c can be associated with pinning mechanisms specific to regions of the applied magnetic field. Research in the literature shows that volume, surface, and point pinning centers are effective in increasing J_c in the low and medium magnetic field region (region up to 4–5 T), but dislocations and strain are effective in the high magnetic field region (> 5 T) [71–74]. When the difference between D650-06 and D650-12 was examined more closely for measurements at 20 K, the J_c ratio was determined as 1.24, 1.32, 1.44, 1.56, 1,97, and 2.01 for each 1 T increase in the range of 0–5 T, respectively. This proportional increase between these two samples in the region of
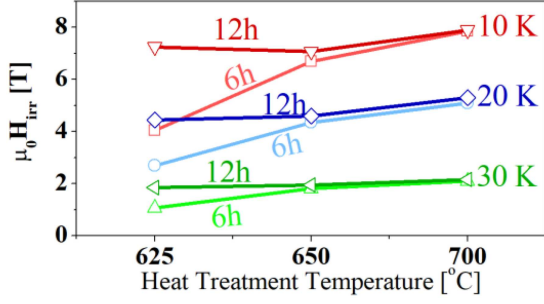
Fig. 8. Magnetic irreversibility field $\mu_0 H_{irr}$ determined from the $J_c = 100$ A/cm^2 criterion.

Fig. 9. Critical current density $J_c(H/H_{irr})$ of the samples at 20 K.

higher magnetic field application suggested that the sample gained a more resistant structure against J_c degradation with increasing field. In this case, the recovery rate of 1.24 in the self-field with increasing HT time was interpreted as an increase in MgB$_2$ phase formation. In the region up to 5 T, it can be said that the surface and point pinning centers are more developed in the 12-h HT example.

When the 6-hour HT data were compared between the heat treatments at 650°C and 700°C, it was clearly seen that higher J_c values could be obtained at 700°C. In the proportional analysis made for 20 K, the J_c ratio for the self-field was observed to be 2 times. However, this ratio increased with increasing magnetic field application and reached 10 times at 5 T. It can be said that the increase in HT temperature develops the pinning centers in the region of the low and medium magnetic field better than the increase in HT time.

Finally, when the 6-h and 12-h HT data at 700°C were compared to each other, no significant difference was detected. The 6-h sample gave slightly better results in the 0–1.5 T region, while the 12-h sample gave partly better results in the 2–5 T region. It was concluded that no significant difference was observed depending on the HT duration both in the 700°C samples and the 650°C samples, and since almost the same J_c curves were obtained, a further increase in the HT duration or temperature would not bring positive results.

The plots of $\mu_0 H_{irr}$ values for different temperatures and HT duration were given in Fig. 8. Here, it was observed that 6 h of HT application at 625°C was an inadequate application with the lowest H_{irr} values. In turn, the application at 625°C for 12 h increased the H_{irr} values. On the other hand, longer HT application in the 650°C and 700°C samples did not have as great an effect as at 625°C. Additionally, the difference between the samples heated at 650°C and 700°C was observed to be very small. Accordingly, in terms of H_{irr}, we can say that while increasing the HT time provides slightly better structure in the 650°C samples, similar structures are formed in the 700°C samples. This result is in agreement with our previous findings.
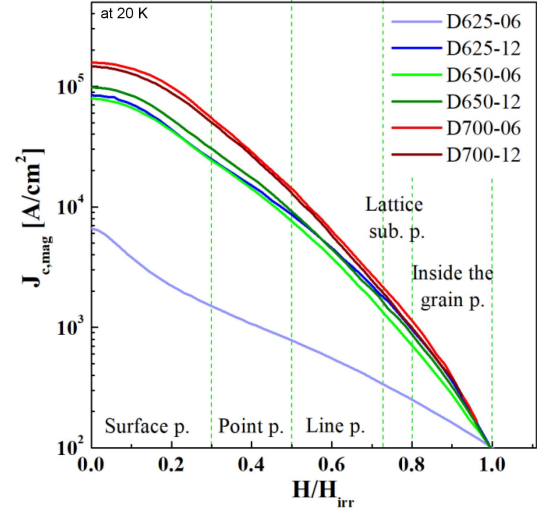
At this point, it was decided to examine the pinning mechanism to better understand the changes in the J_c curves. In order to describe the pinning mechanism in detail, the flux pinning force (F_p) was obtained from the J_c values using the formula $\boldsymbol{F_p} = \boldsymbol{J_c} \times \boldsymbol{B}$ [75], where $\boldsymbol{J_c}$ is the critical current density along the wire, and $\boldsymbol{B}$ is the applied magnetic field perpendicular to the wire length. The fact that the F_p peak occurs in low fields is due to the strong decrease in $J_c(B)$ as you move up to higher fields. The Dew-Hughes (DH) scaling approach [76] was used to compare the pinning mechanisms in our samples. To determine the pinning mechanism, flux pinning diagrams were simulated using the Dew-Hughes equation

$$f_p = A \, (h)^p \, (1 - h)^q \,, \tag{5}$$

where the flux pinning force density was normalized as $f_p = F_p/F_{p,\max}$ and the magnetic field reduced as $h = H/H_{irr}$. According to Dew-Hughes, the h value at which the peak is observed in the f_p versus h graphs indicates the type of pinning mechanism in the produced material. In the DH equation, p and q describe the actual pinning mechanism, and A is a numerical parameter [76–78].

In the Dew-Hughes approach, the value of $F_{p,\max}$ is needed to calculate the normalized flux pinning force, and the value of H_{irr} is needed for the reduced magnetic field. In the magnetization measurements of the samples in this study, there are flux jumps at 5 K, making it difficult to accurately determine the value of $F_{p,\max}$. In addition, possible errors arising from the calculations are multiplied in the F_p values produced by calculation based on the J_c values calculated with the Bean model from the $M(H)$ curves. For these reasons, it is envisaged that examining the J_c values according to the reduced magnetic field with the method suggested by Gajda [79] will reduce these errors.

In fact, the method described in [79] complements previous methods and allows for a better analysis of high-field stabilization centers in MgB_2 wires. In this method, instead of $F_{p,\max}$, graphs of J_c versus B/B_{irr} are directly created. In these graphs, certain B/B_{irr} values correspond to certain pinning mechanisms. Accordingly, the dominant mechanism in the range $0.00 < B/B_{irr} < 0.33$ originates from the surface pinning centers. The dominant mechanism in the range of $0.30 < B/B_{irr} < 0.50$ originates from the point pinning centers. The dominant mechanism in the range $0.50 < B/B_{irr} < 0.75$ is due to line pinning centers. The dominant mechanism in the range $0.75 < B/B_{irr} < 0.80$ is due to the substitution of pinning centers in the crystal lattice, and Gajda [79] reported that the equation $(b)^{2.3-3.9}(1-b)^1$ describes this type of pinning mechanism well. Finally, it was reported that in the range of $0.80 < B/B_{irr} < 1.00$, the pinning centers responsible for the peak effect are active, and equation $(b)^{4.9}(1-b)^1$ describes this type of pinning mechanism well [79]. When Fig. 9 is examined closely, it can be seen that J_c in samples D625-12, D650-06, and D650-12 is decreased by 69% in the ranges from 0.1 to 0.3 and from 0.3 to 0.5. This suggests that samples D625-12, D650-06, and D650-12 have a similar number of surface and point pinning centers. The critical current density J_c in sample D625-06 is decreased by 75% in the range 0.1–0.3 and 45% in the range 0.3–0.5. This suggests that samples D625-06 have more point pinning centers than surface pinning centers. In samples D700-06 and D700-12, J_c is decreased by 65% in the range 0.1–0.3 and 76% in the range 0.3–0.5. This suggests that samples D700-06 and D700-12 have more surface pinning centers than point pinning centers. On the other hand, J_c in all samples is reduced by 80% in the range 0.5–0.74 and 50% in the range 0.74–0.8 (Fig. 3). This indicates that all samples have only a small number of high-field pinning centers.

4. Conclusions

MgB_2, which is an important candidate for future technology due to its high transition temperature, attracts special attention in areas such as portable applications, space applications, transportation, medicine, and energy, thanks to its lightness. In this study, we focused on the production of MgB_2 by the Mg diffusion method for applications requiring high particle bonding because we believe that material properties should be evaluated and developed according to the needs of the applications. The effects of production by the Mg diffusion method at different temperatures and times on polycrystalline MgB_2 bulk superconductors were examined. In particular, the phase formations and crystal structure properties were examined in detail by refining the XRD patterns with the Fullprof software, the microstructure by examining SEM images, and the material behavior under the applied magnetic field by analyzing the $M(H)$ and $M(T)$ graphs. It was determined that there was basically a two-phase structure, and the MgO ratio as the secondary phase was limited to 2%. Additionally, the lattice parameter a of MgB_2 polycrystal was determined to be in the range of 3.0828–3.0864 Å, and the lattice parameter c was determined to be in the range of 3.5206–3.5255 Å. The crystal size was calculated according to the WH model — the optimum crystal size was reached as a result of HT applied for 12 h at 650°C. In SEM images of the produced samples, it was seen that the 650°C and 700°C samples showed similar structures and had better grain connections than the 625°C samples. This result was also supported by $M(T)$ measurements. Despite the small differences between the critical temperature values determined from $M(T)$ measurements between the 650°C and 700°C samples, the sharp phase transition of these samples showed that these samples exhibited a good degree of homogeneity. According to the Bean model, it was seen from the hysteresis curves that the samples exhibited a critical current density (J_c) of up to 10^5 A/cm^2 at 10 K. Additionally when the pinning mechanism in the sample was examined using the Dew-Hughes approach, it was observed that grain boundaries acted as pinning centers and developed with increasing HT temperature. It has been observed that applying the Mg diffusion method at 650°C for 6–12 h dwell time can provide optimum conditions for technological applications that require a good connection between grains.

Acknowledgments

References

[1] J. Nagamatsu, N. Nakagawa, T. Muranaka, Y. Zenitani, J. Akimitsu, *Nature* **410**, 63 (2001).

[2] K. Singh, R. Mohan, N. Kaur, N.K. Gaur, M. Dixit, V. Shelke, R.K. Singh, *Physica C* **450**, 124 (2006).

[3] C. Fischer, W. Häßler, C. Rodig, O.Perner, G. Behr, M. Schubert, K. Nenkov, J. Eckert, B. Holzapfel, L. Schultz, *Physica C* **406**, 121 (2004).

[4] K. Yamazaki, S.H. Risbud, H. Aoyama, K. Shoda, *J. Mater. Process. Technol.* **56**, 955 (1996).

[5] D.K. Kang, D.W. Kim, S.H. Choi, C.J. Kim, I.S. Ahn, *Met. Mater. Internat.* **15**, 15 (2009).

[6] N.M. Hapipi, S.K. Chen, A.H. Shaari, M.M.A. Kechik, K.P. Lim, K.B. Tan, O.J. Lee, S.S. Arvapalli, M. Miryala, *J. Mater. Sci. Mater. Electron.* **33**, 11257 (2022).

[7] P.P.K. Agarwal, T. Matsoukas, *ACS Appl. Energy Mater.* **5**, 5310 (2022).

[8] S. Barua, M.S.A. Hossain, Z. Ma et al., *Scr. Mater.* **104**, 37 (2015).

[9] G. Giunchi, G. Ripamonti, T. Cavallin, E. Bassani, *Cryogenics* **46**, 237 (2006).

[10] A. Bhagurkar, Ph.D. Thesis, Brunel Univeristy London, 2017.

[11] S.S. Arvapalli, M. Miryala, M. Jirsa, N. Sakai, M. Murakami, *J. Supercond. Novel Magn.* **34**, 1297 (2021).

[12] A.G. Bhagurkar, A. Yamamoto, L. Wang, M. Xia, A.R. Dennis, J.H. Durrell, T.A. Aljohani, N.H. Babu, D.A. Cardwell, *Sci. Rep.* **8**, 13320 (2018).

[13] D. Zhang, Z.K. Wang, S.T. Dai et al., *IEEE Tran. Appl. Supercond.* **20**, 764 (2010).

[14] V. Braccini, D. Nardelli, R. Penco, G. Grasso, *Physica C* **456**, 209 (2007).

[15] A. Serquis, L. Civale, J.Y. Coulter, D.L. Hammon, X.Z. Liao, Y.T. Zhu, D.E. Peterson, F.M. Mueller, V.F. Nesterenko, S.S. Indrakanti, *Supercond. Sci. Technol.* **17**, L35 (2004).

[16] A.A. Amin, T.N. Baig, R.J. Deissler, L.A. Sabri, D. Doll, M. Tomsic, O. Akkus, M.A. Martens, *IEEE Trans. Appl. Supercond.* **27**, 4602205 (2017).

[17] D. Mijatovic, A. Brinkman, D. Veldhuis et al., *Appl. Phys. Lett.* **87**, 192505 (2005).

[18] S.A. Cybart, K. Chen, Y. Cui, Q. Li, X.X. Xi, R.C. Dynes, *Appl. Phys. Lett.* **88**, 012509 (2006).

[19] K. Chen, Y. Cui, Q. Li, X.X. Xi, S.A. Cybart, R.C. Dynes, X. Weng, E.C. Dickey, J.M. Redwing, *Appl. Phys. Lett.* **88**, 222511 (2006).

[20] Ö. Çiçek, K. Yakıncı, *J. Mater. Electron. Devices* **4**, 30 (2023).

[21] E. Bayazit, M.E. Yakinci, Y. Balci, M.A. Aksan, *Physica C* **460–462**, 610 (2007).

[22] A. Ballarino, R. Flükiger, *J. Phys. Conf. Ser.* **871**, 012098 (2017).

[23] M.E. Yakinci, Y. Aydogdu, M.A. Aksan, Y. Balci, S. Altin, *J. Supercond. Novel Magn.* **24**, 241 (2011).

[24] E. Altin, F. Kurt, S. Altin, M.E. Yakinci, Z.D. Yakinci, *Curr. Appl. Phys.* **14**, 245 (2014).

[25] J.G. Noudem, Y. Xing, P. Bernstein, R. Retoux, M. Higuchi, S.S. Arvapalli, M. Muralidhar, M. Murakami, *J. Am. Ceram. Soc.* **103**, 6169 (2020).

[26] M. Alessandrini, H. Fang, M. Hanna, P.Putman, Y.X. Zhou, K. Salama, *Supercond. Sci. Technol.* **19**, 129 (2005).

[27] G. Gajda, A. Morawski, K. Rogacki, *Supercond. Sci. Technol.* **29**, 095002 (2016).

[28] A. Serquis, L. Civale, D.L Hammon, X.Z. Liao, J.Y. Coulter, Y.T. Zhu, M. Jaime, D.E. Peterson, F.M. Mueller, V.F. Nesterenko, Y. Gu, *Appl. Phys. Lett.* **82**, 2847 (2003).

[29] G. Kirat, O. Kizilaslan, M.A. Aksan, M.E. Yakinci, *Physica B* **445**, 24 (2014).

[30] M. Miryala, S.S. Arvapalli, P. Diko, M. Jirsa, M. Murakami, *Adv. Eng. Mater.* **22**, 1900750 (2019).

[31] Y. Yang, M.D. Sumption, M. Rindfleisch, M. Tomsic, E.W. Collings, *Supercond. Sci. Technol.* **34**, 025010 (2021).

[32] S.X. Dou, O. Shcherbakova, W.K. Yeoh et al., *Phys. Rev. Lett.* **98**, 139902 (2007).

[33] D. Bumin, E. Yanmaz, M. Basoglu, A. Gencer, *J. Supercond. Novel Magn.* **24**, 211 (2011).

[34] M. Burdusel, G. Aldica, S. Popa, M. Enculescu, V. Mihalache, A. Kuncser, I. Pasuk, P. Badica, *Curr. Appl. Phys.* **15**, 1262 (2015).

[35] D.K. Wong, W.K. Yeoh, K.B. De Silva et al., *J. Alloys Compd.* **644**, 900 (2015).

[36] I. Ahmad, J.S. Hansdah, S.N. Sarangi, M. Sarun, *J. Alloys Compd.* **834**, 155033 (2020).

[37] M.G. Babaoğlu, S. Safran, Ö. Çiçek, H. Ağıl, E. Ertekin, M.S.A. Hossain, E. Yanmaz, A. Gencer, *J. Magn. Magn. Mater.* **324**, 3455 (2012).

[38] M.S.A. Hossain, A. Motaman, Ö. Çiçek, H. Ağıl, E. Ertekin, A. Gencer, X.L. Wang, S.X. Dou, *Cryogenics* **52**, 755 (2012).

[39] A. Vajpayee, R. Jha, A.K. Srivastava, H. Kishan, M. Tropeano, C. Ferdeghini, V.S.P. Awana, *Supercond. Sci. Technol.* **24**, 045013 (2011).

[40] S. Hata, H. Sosiati, Y. Shimada, A. Matsumoto, K. Ikeda, H. Nakashima, H. Kitaguchi, H. Kumakura, *J. Mater. Sci.* **48**, 132 (2013).

[41] B.A. Glowacki, M. Majoros, M.E. Vickers, B. Zeimetz, *Physica C* **372–376**, 1254 (2002).

[42] T. Matsushita, M. Kiuchi, A. Yamamoto, J.-i. Shimoyama, K. Kishio, *Supercond. Sci. Technol.* **21**, 015008 (2007).

[43] K. Onar, Y. Balci, M.E. Yakinci, *J. Mater. Sci. Mater. Electron.* **25**, 2104 (2014).

[44] H. Yanrong, P. Xifeng, Y. Guo, W. Dayou, C. Lijun, F. Jianqing, F. Yong, *Rare Metal Mater. Eng.* **47**, 1406 (2018).

[45] S. Ueda, J.-i. Shimoyama, I. Iwayama, A. Yamamoto, Y. Katsura, S. Horii, K. Kishio, *Appl. Phys. Lett.* **86**, 222502 (2005).

[46] H. Kobayashi, M. Muralidhar, M.R. Koblischka, K. Inoue, M. Murakami, *Phys. Proc.* **65**, 73 (2015).

[47] D. Gajda, A.J. Zaleski, A. Morawski, T. Czujko, D. Avci, F. Karaboga, M. Akdogan, H. Yetis, T. Cetner, I. Belenli, *J. Alloys Compd.* **889**, 161665 (2021).

[48] G.Z. Li, M.D. Sumption, E.W. Collings, *Acta Mater.* **96**, 66 (2015).

[49] D. Gajda, A.J. Zaleski, M. Babij, D. Szymański, A.J. Morawski, M.A. Rindfleisch, D. Patel, M.S.A. Hossain, *J. Alloys Compd.* **963**, 171239 (2023).

[50] G.K. Williamson, W.H. Hall, *Acta Metall.* **1**, 22, (1953).

[51] C.P. Bean, *Phys. Rev. Lett.* **8**, 250 (1962).

[52] J.L. Dadiel, J. Sugiyama, N. Sakai, K. Takemura, T. Oka, H. Ogino, M. Muralidhar, M. Murakami, *J. Supercond. Novel Magn.* **36**, 1097 (2023).

[53] C.F. Liu, G. Yan, S.J. Du, W. Xi, Y. Feng, X. Zhang, X.Z. Wu, L. Zhou, *Physica C* **386**, 603 (2003).

[54] H. Tanaka, A. Yamamoto, J.-i. Shimoyama, H. Ogino, K. Kishio, *Supercond. Sci. Technol.* **25**, 115022 (2012).

[55] Y. Shimada, Y. Kubota, S. Hata, K. Ikeda, H. Nakashima, A. Matsumoto, K. Togano, H. Kumakura, *Physica C* **471**, 1137 (2011).

[56] N. Varghese, K. Vinod, A. Rao, Y.K. Kuo, U. Syamaprasad, *J. Alloys Compd.* **470**, 63 (2009).

[57] W. Zhao, H.L. Suo, S. Wang, L. Ma, L. Wang, Q. Wang, Z. Zhang, *J. Eur. Ceram. Soc.* **42**, 7036 (2022).

[58] V.P.S. Awana, A. Vajpayee, M. Mudgel, V. Ganesan, A.M. Awasthi, G.L. Bhalla, H. Kishan, *Eur. Phys. J. B* **62**, 281 (2008).

[59] J.H. Lim, S.H. Jang, S.M. Hwang, J.H. Choi, J. Joo, W.N. Kang, C. Kim, *Physica C* **468**, 1829 (2008).

[60] S. Zhou, A.V. Pan, S.X. Dou, *J. Alloys Compd.* **487**, 42 (2009).

[61] B.B. Sinha, M.B. Kadam, M. Mudgel, V.P.S. Awana, H. Kishan, S.H. Pawar, *Physica C* **470**, 25 (2010).

[62] K. Husekova, I. Husek, P. Kovac, M. Kulich, E. Dobrocka, V. Strbik, *Physica C* **470**, 331 (2010).

[63] Z. Zhang, H. Suo, L. Ma, T. Zhang, M. Liu, M. Zhou, *Physica C* **471**, 908 (2011).

[64] D. Tripathi, T.K. Dey, *J. Alloys Compd.* **618**, 56 (2015).

[65] J.H. Kim, S.X. Dou, M. Rindfleisch, M. Tomsic, *Supercond. Sci. Technol.* **20**, 1026 (2007).

[66] H. Durmuş, K. Kocabaş, *J. Mater. Sci. Mater. Electron.* **33**, 17079 (2022).

[67] C. Tarantini, H.U. Aebersold, V. Braccini et al., *Phys. Rev. B* **73**, 134518 (2006).

[68] B. Lorenz, O. Perner, J. Eckert, C.W. Chu, *Supercond. Sci. Technol.* **19**, 912 (2006).

[69] I. Felner, V.P.S. Awana, M. Mundgel, H. Kishan, *J. Appl. Phys.* **101**, 09G101 (2007).

[70] M. Shadab, M. Jirsa, M. Miryala, *Mater. Chem. Phys.* **309**, 128348 (2023).

[71] D. Gajda, A. Zaleski, A. Morawski, M.S.A. Hossain, *Supercond. Sci. Technol.* **30**, 085011 (2017).

[72] G. Gajda, A. Morawski, R. Diduszko, T. Cetner, M.S.A. Hossain, K. Gruszka, D. Gajda, P. Przyslupski, *J. Alloys Compd.* **709**, 473 (2017).

[73] X. Xu, S.X. Dou, X.L. Wang, J.H. Kim, J.A. Stride, M. Choucair, W.K. Yeoh, R.K. Zheng, S.P. Ringer, *Supercond. Sci. Technol.* **23**, 085003 (2010).

[74] D. Gajda, A. Morawski, A.J. Zaleski, M. Akdoğan, H. Yetiş, F. Karaboğa, T. Cetner, İ. Belenli, *J. Supercond. Novel Magn.* **30**, 3397 (2017).

[75] M.R. Koblischka, M. Murakami, *Supercond. Sci. Technol.* **13**, 738 (2000).

[76] D. Dew-Hughes, *Philos. Mag.* **30**, 293 (1974).

[77] M. Santosh, A. Sai Srikanth, M. Muralidhar, *Supercond. Novel Magn.* **35**, 2785 (2022).

[78] Y. Xing, P. Berntein, M. Muralidhar, *J. Noudem, Supercond. Sci. Technol.* **36**, 115005 (2023).

[79] D. Gajda, *J. Low Temp. Phys.* **194**, 166 (2019).